Summary of the 27th IAEA Fusion Energy Conference in the categories of EX/W, EX/D, and ICC

Summary of 27th IAEA Fusion Energy Conference in the categories of EX/W, EX/D, and ICC

K. Ida[1, 2]

[1]National Institute for Fusion Science, National Institutes of Natural Sciences, Toki, Gifu 509-5292, Japan
[2]SOKENDAI (The Graduate University for Advanced Studies), Toki, Gifu 509-5292, Japan

(Dated: August 1, 2019)

This is a summary paper of the 27th IAEA Fusion Energy Conference which was held from 22 - 27 October 2018 in Ahmedabad, India. The results in the categories of EX/W (wave-plasma interactions, current drive, heating, energetic particles), EX/D (plasma-material interactions, divertors, limiters, scrape-off layer (SOL)), and ICC (innovative confinement concepts) in magnetic confinement experiments are summarized. In total, 121 papers have been contributed to these categories. Interesting results on the coupling between energetic particles, MHD, wave-particle interaction, turbulence, SOL physics, and divertor are presented at this conference. For example, control of energetic particle driven MHD by electron cyclotron heating and resonance magnetic perturbation, mitigation of disruption by energetic particle driven MHD, control of decay length by SOL turbulence, and wave scattering by SOL density fluctuations were discussed in this conference. Deeper understanding of these couplings will be essential for the sustainment of high performance steady-state plasma in ITER.

PACS numbers:

I. INTRODUCTION

The 27th International Atomic Energy Agency (IAEA) Fusion Energy Conference (FEC) was held from 22 - 27 October 2018, in Ahmedabad, India. This conference aims to provide a forum for the discussion of key physics and technology issues as well as innovative concepts of direct relevance to the use of nuclear fusion as a source of energy. The scientific scope of the FEC 2018 is, therefore, intended to reflect the priorities of this new era in fusion energy research. The conference aims to serve as a platform for sharing the results of research and development efforts in both national and international fusion experiments that have been shaped by these new priorities, and to thereby help in pinpointing worldwide advances in fusion theory, experiments, technology, engineering, safety and socio-economics. Furthermore, the conference will also set these results against the backdrop of the requirements for a net energy producing fusion device and a fusion power plant in general, and will thus help in defining the way forward.

The FEC 2018 consists of 4 keynote presentations, 24 overview talks, 78 regular talks, 17 rapporteur papers, 11 overview poster presentations, 518 regular poster presentations, and 5 summary talks over 6 days. The total number of participants was close to one thousand. The topics of this conference are 1:Magnetic Confinement Experiments (EX), 2:Magnetic Confinement Theory and Modelling (TH), 3:Plasma Overall Performance and Control) (PPC), 4:Inertial Fusion Experiments and Theory (IFC), 5:Innovative Confinement Concepts (ICC), 6:Fusion Engineering, Integration and Power Plant Design (FIP), 7:Fusion Nuclear Physics and Technology (FNS), 8:Materials Physics and Technology (MPT), and 9:Safety, Environmental and Economic Aspects of Fusion (SEE). There are four subtopics in the topics of Magnetic Confinement Experiments (EX) and Magnetic Confinement Theory and Modelling (TH) and the subtopics are 1:Confinement (C), 2:Stability (S), 3:Wave-plasma interactions, current drive, heating, energetic particles (W), and 4:plasma-material interactions, divertors, limiters, SOL (D). The results presented on these topics in this conference were summarized on the last day of the conference by the following five speakers: Dr. David Campbell (topics EX/C, EX/S & PPC), Dr. Katsumi Ida (topics EX/D, EX/W & ICC), Prof. Ricardo Galvao (topics Magnetic Confinement Theory), Dr. Radha Bahukutumbi (topics Inertial Fusion Experiments and Theory), and Dr. Takashi Inoue (topics FIP, FNS, MPT & SEE).

In this paper, results in the categories of EX/W (wave-plasma interactions, current drive, heating, energetic particles), EX/D (plasma-material interactions, divertors, limiters, scrape-off layer (SOL)), and ICC (innovative confinement concepts) in magnetic confinement experiments are summarized. In total, 121 papers have contributed to these categories. Interesting results on the coupling between energetic particle, MHD, wave-particle interaction, turbulence, SOL physics, and divertor are presented at this conference. For example, control of energetic particle driven MHD by electron cyclotron heating and resonance magnetic perturbation, mitigation of disruption by energetic particle driven MHD, control of decay length by SOL turbulence, and wave scattering by SOL density fluctuations are discussed in this conference. Deeper understanding of these couplings would be essential for the sustainment of high performance steady-state plasma in ITER.

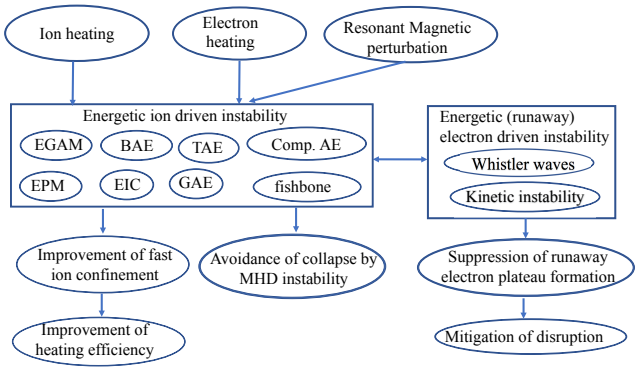

FIG. 1: Diagram of physics element in the field of wave-plasma interactions, current drive, heating and energetic particles.

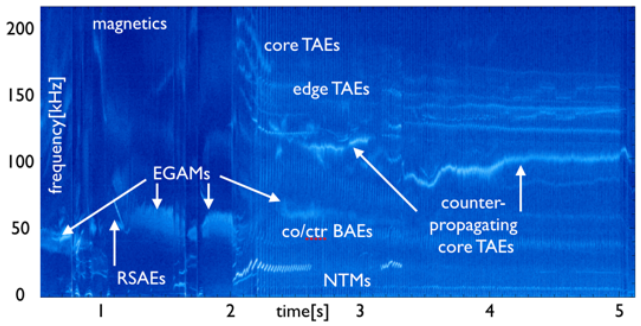

FIG. 2: Time evolution of magnetic fluctuations of ASDEX Upgrade discharge #34924. (Adapted from figure 1 in [1]).

II. WAVE-PLASMA INTERACTIONS, CURRENT DRIVE, HEATING, ENERGETIC PARTICLES

A. Energetic particle (EP) driven instability

Figure 1 shows a diagram of physics elements in the field of wave-plasma interactions, current drive, heating, energetic particle. The electron cyclotron heating (ECH) and resonant magnetic perturbation (RMP) field have a significant impact on the energetic ion driven instability. Energetic particle (EP)-driven geodesic acoustic mode (EGAM), beta-induced Alfvén eigenmode (BAE), toroidal Alfvén eigenmode (TAE), compressional Alfvén eigenmode (comp. AE), energetic particle mode (EPM), Energetic particle driven resistive InterChange mode (EIC), global Alfveń eigenmode (GAE), and fishbone are in this group. The other group is energetic electron (runaway electron) driven instabilities such as whistler wavesand kinetic instabilities. The suppression of the energetic ion driven instability is needed for the improvement of fast-ion confinement and heating efficiency as a result. Because the abrupt loss of thermal kinetic energy is triggered by these instabilities, the suppression of the energetic ion driven instability contributes to the avoidance of plasma collapse. The important findings are the fact that various EP-driven instability appears simultaneously when the beam pressure is comparable to the bulk pressure. The reason the community is interested in these scenarios with large β_{EP} is that various non-linear saturation mechanisms appear at large β_{EP} that need to be understood by theory, captured by numerical models, validated by code-experiment comparisons and then used for the prediction of burning plasmas.

Observation of the various energetic particle (EP) driven instability has been reported from ASDEX Upgrade. Figure 2 shows various energetic particle (EP) driven instabilities simultaneously observed in ASDEX Upgrade : EP-driven geodesic acoustic modes (EGAMs), beta-induced Alfvén eigenmodes (BAEs), reversed shear Alfvén eigenmodes (RSAEs) and toroidal Alfvén eigenmodes (TAEs) that are modulated by transient q = 2 sawtooth-like crashes, neoclassical tearing mode (NTM) and edge localized mode (ELM) [1]. It was reported that one EP driven instability triggers the other EP driven instability. For example, TAE bursts are observed to trigger the onset of EGAMs which indicates coupling of these modes via the velocity space (EP avalanches) and via mode-mode coupling processes. It is an important finding that several EP driven instabilities can be co-exist in the plasma when the energetic particle pressure generated by neutral beam is comparable to the background plasma pressure. A crucial point of this paper was that $E_{beam}/Ti, e_{thermal}$ was ~ 100, as in a burning plasma. This was reached via keeping low background temperatures (core tungsten accumulation) despite 5MW NBI heating. In the plasma with high fraction of energetic particle pressure, interactions among EP instability becomes more significant due to the non-linear coupling between the different EP driven instability. Bicoherence analysis reveals the non-linear coupling processes between different frequency bands.

Observation of various high-frequency modes driven by energetic anisotropic fast ions or runaway electrons are reported from DIII-D, which is summarized in figure 3 [2–5]. High-frequency modes observed in the DIII-D tokamak have been identified as energetic particle instability driven by anisotropic fast ions or runaway electrons. Doppler-shifted cyclotron resonant compressional Alfvén Eigenmodes (CAEs) with frequencies f less than the main ion cyclotron frequency f_{ci} are measured and many aspects of observation are consistent with CAE theory. CAEs are excited on DIII-D when the beam ions are

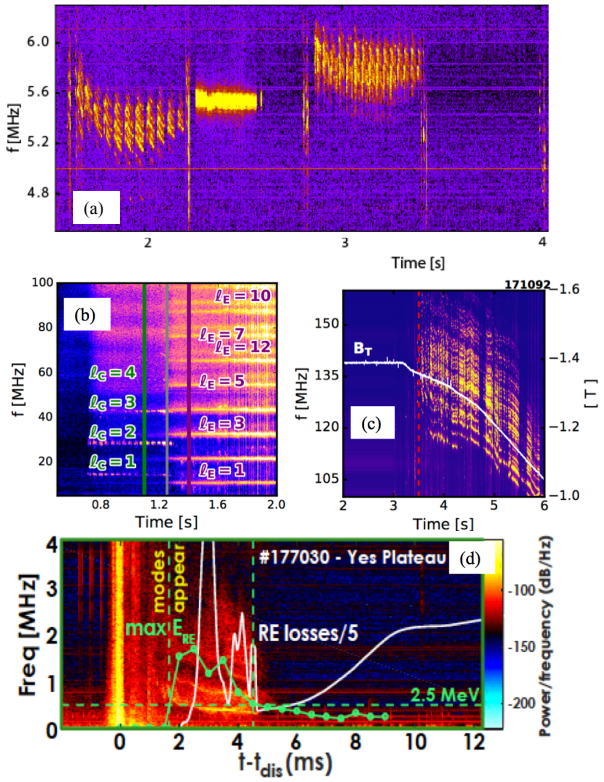

FIG. 3: Time evolution of magnetic fluctuations of DIII-D discharge for (a) compressional Alfvén eigenmodes (CAEs), (b) collective ion cyclotron emission (ICE), (c) whistler wave excited by runaway electrons, and (d) mode that suppresses runaway beam. (Adapted from figure 1(b) in [2], figure 5(a) in [3], 6(c) in [2] and figure 3(b) in [5]).

near-Alfvénic, with onset frequencies of $\sim 0.6 f_{ci}$. Ion cyclotron Emission (ICE) is readily excited across a wide region of operational space by kinetic instability at harmonics of the main ion f_{ci}. ICE is strongest in neutral-beam-heated plasma with a clear dependence on beam geometry, with the highest emission levels with counter-current beams. Whistler waves with $f >> f_{ci}$, excited by multi-MeV runaway electrons have been observed in a low-density ($n_e \sim 10^{19}\mathrm{m}^{-3}$) tokamak plasma [6]. The waves occur in multiple discrete frequency bands in the 100-200 MHz range, with the measured whistler frequencies scaling with magnetic field strength, as expected from the whistler dispersion relation. Another electron-drive mode with $f \sim 0.1 f_{ci}$ has recently been observed that correlates with runaway losses and formation suppression of a runaway beam. The observation of whistler wave excited by energetic electrons (runaway electron) is reported in tokamak plasmas for the first time.

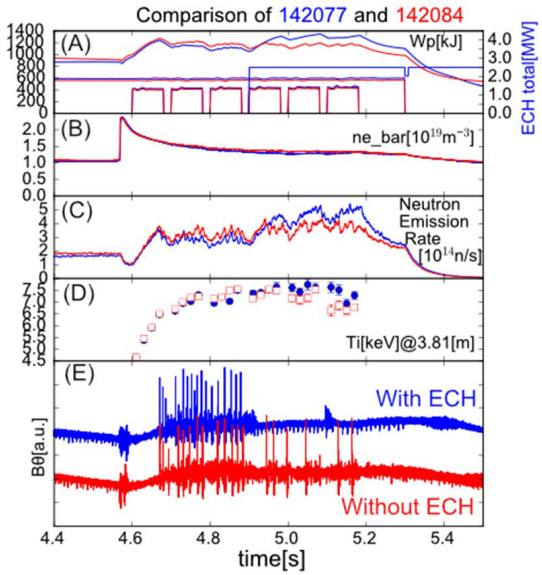

FIG. 4: Time evolution of (A) stored energy of the plasma and heating patterns, (B) time evolution of the line density, (C) the total neutron emission rate, (D) central ion temperature, and (E) the magnetic fluctuations in the discharge with ECH (#142077 blue) and without ECH (#142084 red) in LHD. (Adapted from figure 5 in [7]).

B. ECH effect on EP-driven instability

Many observations that suggest the effective suppression of EP-driven instability by electron cyclotron heating (ECH) have been reported at this conference. Various EP-driven instability disappears when the ECH is applied in both helical and tokamak plasma. It is confirmed that the on-axis ECH is quite effective for suppressing the EP-driven instability (EIC) in the experiments in deuterium plasma as seen in Large Helical Device (LHD) in figure 4 [7]. ECH is changing the stability properties of the EIC modes (interchange physics) and thus the ECH indirectly increases the EP population since the EP transport due to the EIC mode is now suppressed. This EP-driven instability appears when the energetic ion pressure, especially trapped particle ion pressure, becomes high enough by injecting perpendicular beam ($\sim$ 10 MW total) into the low density plasma of $n_e \sim 10^{19}\mathrm{m}^{-3}$. The perpendicular beam is injected from $t = 4.6$ sec, and the ECH is injected from $t = 4.9$ sec. The total neutron emission rate dominated by the beam-plasma reaction increases after the ECH pulse is applied, which demonstrate that the ECH is useful to increase the population of energetic ion from the neutral beams by suppressing the EP-driven instability. The ion temperature only slightly increases by suppressing the EP-driven instability. These observations indicate that

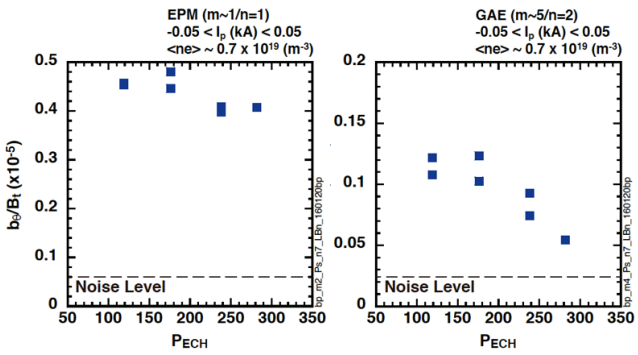

FIG. 5: Dependence of (a) energetic particle modes (EPM) and (b) global Alfvén eigenmodes GAE amplitude of ECH injection power PECH in NBI-heated Heliotron J plasma. (Adapted from figure 7 in [8]).

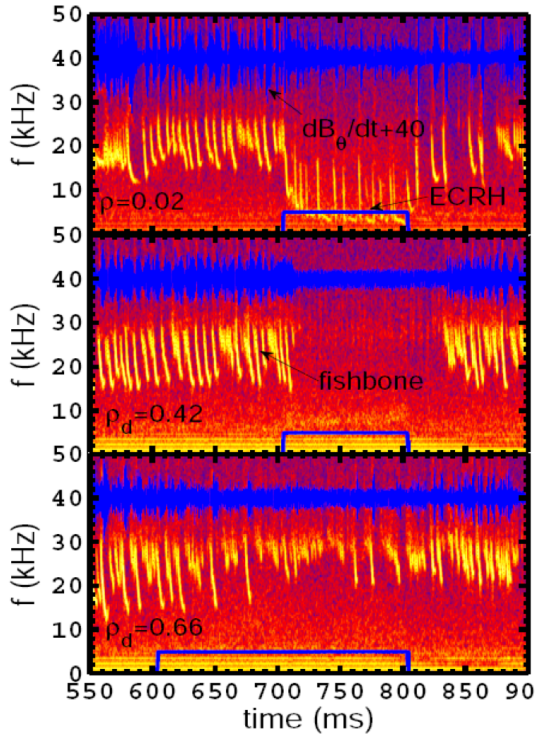

FIG. 6: Effects of ECRH power and the deposition position on the stabilization of ion fishbone activities in HL-2A in dependence of ECH radial deposition location ρ. (Adapted from figure 11 in [9]).

the impact of EP-driven instability on fast ion pressure is larger than that on bulk ion pressure.

The ECH effect on energetic particle modes (EPMs) and global Alfvén eigenmodes (GAEs) is reported from Heliotron J [8]. ECH power is scanned from 120 kW to 280 kW shot by shot to study the influence of ECH on EP-driven instability. As seen in figure 5, the EPM amplitude is only slightly decreased as the ECH power with on-axis heating is increased. However, GAE amplitude is only slightly reduced with the increase of on-axis ECH power. The impact of ECH on GAE amplitude depends on the location of the ECH deposition. As the ECH deposition location approaches to the GAE location at r/a ~0.6, the GAE amplitude becomes larger. This dependence indicates that both the change of fast ion profile by ECH through the change of electron density and temperature, and/or the collisional damping due to trapped fast electrons may affect the AE stability.

Suppression of EP-driven instability by ECH is also observed in the various experiments in tokamaks. The stabilization of m/n=1/1 ion fishbone activities by electron cyclotron heating (ECH) was reported from HL-2A [9]. By scanning the ECH configuration parameters, it was found that the fishbone stability depends not only on the injected power, but also on the radial deposition position of ECRH, which is similar to finding that suppression of EP-driven instability depends on both ECH power and ECH deposition location in Heliotron J. The fishbone can be completely suppressed when the injected ECH power level exceeds a certain threshold. Figure 6 shows the time evolution of magnetic field fluctuation spectra at the ECH power level ($P_{ECH} \sim 1$ MW) above the threshold. When the ECRH power is deposited on-axis (ρ ~0), the observed mode frequency obviously decreases, but the mode amplitude is only weakly reduced. When the power is deposited at ρ ~0.42 outside of the q=1 rational surface (ρ ~0.38), the mode is fully stabilized. However, the mode is partially stabilized when the power is deposited off-axis (ρ ~0.66). This experiment clearly shows that the control of the location of the ECH deposition is quite important to suppress the EP-driven instability effectively.

The correlation of toroidal Alfvén eigenmodes (TAEs) with ECH injection was reported from KSTAR [10]. Figure 7 shows the total neutron rate, stored energy, and β poloidal, for the normal(18597) and high β_p H-modes(18602) and the time evolution of magnetic field fluctuation spectra in the discharge with ECH. During the ECH off phase (t =14-16 sec), n = 1 (80 kHz) and n =3 (120 kHz) TAEs, which are suppressed during the ECH phase, appears. In this phase, the total neutron

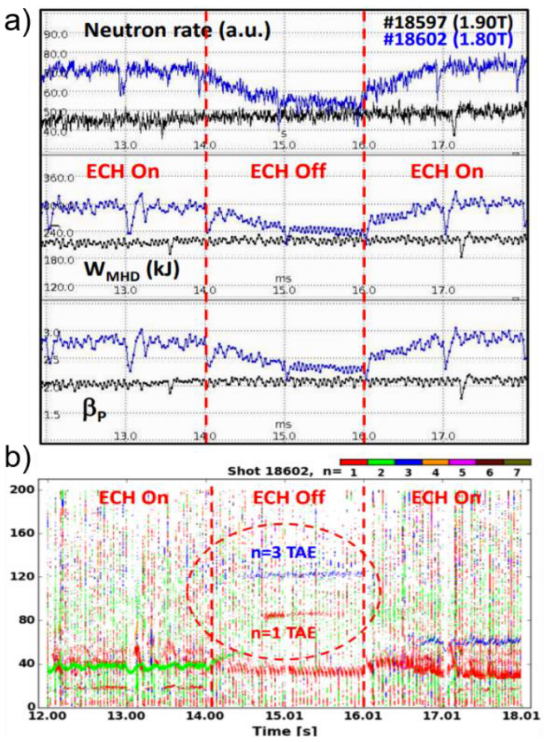

FIG. 7: (a) Time evolution of total neutron rate, stored energy, and β poloidal, for the normal(18597) and high β_p H-modes(18602) and (b) the time evolution of magnetic field fluctuation spectra in the discharge with ECH in high β_p H-modes(18602) in KSTAR. The ECH is turned off only for t =14-16 sec. (Adapted from figure 3(b) in [10]).

emission rate dominated by the beam-target D-D reaction decreases associated with the appearance of TAEs, which suggests the significant decrease of fast ion pressure rather than the bulk plasma pressure similar to the experiment in LHD. The decrease of stored energy and β_p values is also observed during the ECH off phase and this implies the degradation of confinement due to TAEs.

Several experiments in helical and tokamak plasmas provide common results, which are summarized below. 1) EP-driven instability has a significant effect on fast-ion confinement (reducing the fast-ion pressure) rather than bulk confinement. 2) The EP-driven instability can be suppressed by applying ECH with the power above the critical value. 3) The location of the deposition of ECH is important to suppress the EP-driven instability efficiently. Although the mechanism of suppression of EP-driven mode by ECH has been studied in several experiments [11], more detailed investigation for the mechanism is necessary for the development of more efficient techniques for EP-driven instability suppression.

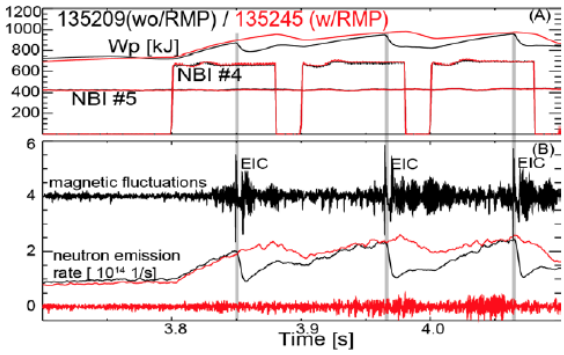

FIG. 8: (A) Comparison of the plasma parameters with and without the RMP field. The time evolution of plasma stored energy with NBI wave form and (B) the magnetic fluctuations and the total neutron emission rate in the discharge without (#135209 black) and with (#135245 red) RMP in LHD. (Adapted from figure 6 in [7]).

C. RMP effect on EP-driven instability

The resonant magnetic perturbation (RMP) has been used for the H-mode discharge to suppress ELM. Recently, the RMP is also applied to suppress the EP-driven instability both in helical and tokamak plasma.

An example of suppression of EP-driven instability (EIC) at $m/n = 1/1$ resonant magnetic field perturbation (RMP) was reported from LHD [7], which is summarized in figure 8. After the additional perpendicular NBI (#4), repeated bursts of magnetic fluctuation (EIC) are observed. Associated with the MHD burst, the neutron emission rate drops, which indicates the loss of trapped fast ions of the beam. Although the drop of stored energy is observed associated with the instability, the drop of stored energy is smaller the drop of the neutron rate, which is mainly provided by the beam-plasma reaction. In the discharge with RMP field, no EP-driven instability and no drop of neutron emission rate associated with the instability is observed. The small decrease of the neutron emission rate in the discharge with RMP is due to the NBI gap in the background measurement of charge exchange spectroscopy. This suppression is observed when the electron density is not too low (line averaged electron density $n_e \sim 0.9 \times 10^{19}$ m^{-3}). Because the magnitude of the perturbation of the magnetic field is too small to affect the orbit of energetic particle, the suppression mechanism of EP driven instability by RMP is not well understood. The stabilization of seed interchange mode and decrease of the gradient of energetic fast ion pressure are the possible candidates for suppression mechanism.

Suppression of EP-driven instability of the RMP was also reported from ASDEX Upgrade (AUG) [12, 13].

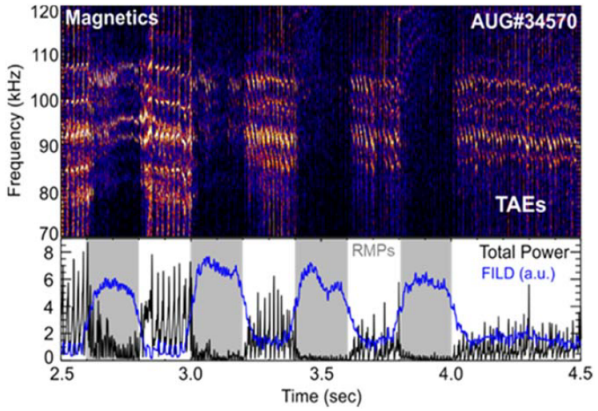

FIG. 9: Magnetic spectrogram and temporal evolution of the root-mean-square (RMS) amplitude of band-pass filtered magnetic fluctuation (black) in TAE frequency together with the fast-ion loss level obtained with the Fast-Ion Loss Detector (FILD) diagnostic (blue) in ASDEX Upgrade. (Adapted from figure 13 in [13]).

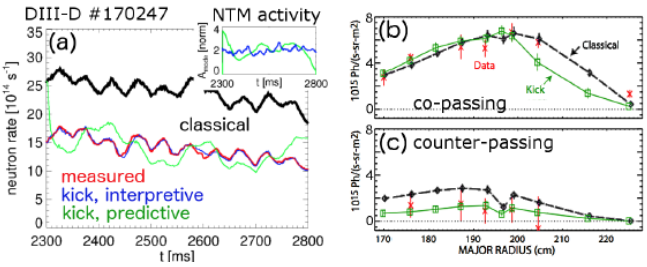

FIG. 10: (a) Time evolution of neutron rate measured and that from TRANSP modeling and radial profile of FIDA signal measured for (b) co- and (c) counter- passing fast ions and that from TRANSP modeling in DIII-D. (Adapted from figure 3(a) in [14] and figure 18(a) and figure 18(b) in [17]).

The NBI driven toroidal Alfvén eigenmode (TAEs) is mitigated or suppressed by RMP.

Figure 9 shows the TAE instability in the frequency range of 70 to 120 kHz measured with a magnetic pick-up coil in AUG. A clear modulation of the TAE instability is observed with the application of externally applied RMP fields. Timing of the applied RMPs is highlighted in the bottom panel with vertical grey stripes. In the bottom panel, the temporal evolution of the root-mean-square (RMS) amplitude of TAE is plotted together with that of the of the measured fast-ion losses. As the discharge evolves in time, the overall TAE activity becomes weaker due to the change in q-profile. RMP blips are clearly modulating and eventually suppressing the TAE instability completely. Fast-ion losses measured with one of the fast-ion loss detectors (FILD) show a clear correlation between applied RMP fields and TAE instability.

It was also found that the phase of RMP is important for the effective suppression of TAE instability by the RMP. Then, two different shots were carried out in which the MPs were applied intermittently with two differential phases corresponding to the maximum and minimum level of fast-ion losses measured by FILD. The RMP phase of $\Delta\phi = 100°$ and $\Delta\phi = 50°$ correspond to the maximum and minimum levels of fast-ion losses, respectively. The modulation of the fast-ion loss level measured by FILD is larger in the discharge with $\Delta\phi = 100°$ than that in the discharge $\Delta\phi = 50°$. This experiment clearly demonstrates that the suppression of EP-driven instability is quite sensitive to the phase of RMP. This is because the fast ion profile, especially the given pitch angle at the edge, is significantly modified depending on the phase of RMP.

D. Energetic particle transport simulation

The validation of the transport model for energetic particle (EP) owing to the EP-driven instability was reported from DIII-D. The transport model for energetic particle (EP) due to the EP driven instability is validated by comparing the experimental data of neutron rate and fast ion D_α (FIDA) signal. As the EP-driven transport model, the kick model has been designed to fit within the Monte Carlo implementation of NUBEAM. The wave-particle interaction process is distilled into kick probability matrix through orbit modeling and the effect of EP transport by instability is included is included into tokamak transport code TRANSP [14–17]. Figure 10 shows time evolution of neutron rate measured and that from TRANSP modeling and radial profile of FIDA signal measured for co- and counter- passing fast ions in DIII-D discharge with large 2/1 NTM oscillation amplitude. The deviation between the measured neutron rate and classical simulation indicates substantial fast ion transport. The neutron rate calculated by using the measured magnetic island width (predictive) and adjusting NTM amplitude (interactive) has good agreement with the measurements. Although there is no velocity space resolution in the neutron rate, FIDA signals provide the information of velocity space. Therefore, comparison of FIDA signals between the measurements and reproduced by the kick model provides more definite validation of the model. Deviations between measured FIDA signal and classical simulation results are much more significant in the counter-passing particle than co-passing particles, which indicate the loss of counter- passing fast ions. The reproduced FIDA signals for the kick model gave good agreement with the measurements of both the co-passing

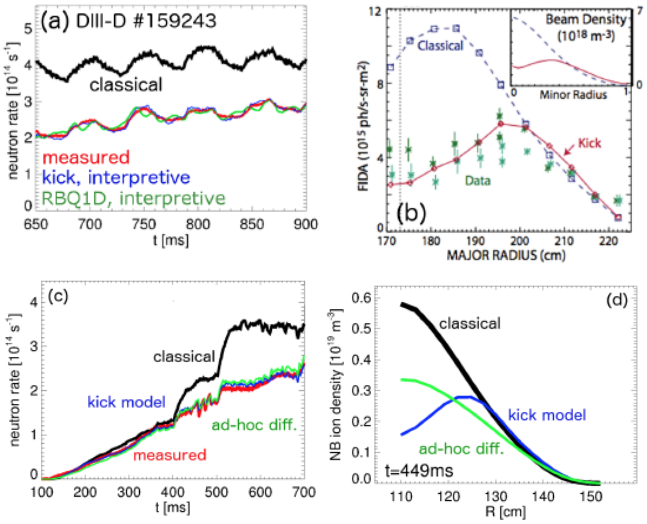

FIG. 11: (a) Time evolution of neutron rate measured and that from TRANSP modeling and (b) radial profile of FIDA signal measured and that from classical and kick model in DIII-D and (c) time evolution of neutron rate and (d) radial profiles of fast-ion density in NSTX-U. (Adapted from figure 11(a) and figure 12 in [18] and figure 1(c) and figure 1(d) from in [15]).

and counter-passing fast ions.

The kick model has also recovered the measured toroidal Alfvén eigenmode (TAE) spectrum of NSTX-U and DIII-D and has reproduced details of fast-ion diagnostics data (neutron rate and FIDA signal). Figure 11 shows the comparison of the measured neutron rate and radial profile of fast ion between the measurements and kick model in DIII-D and NSTX-U discharge [15, 17, 18]. A significant loss of fast ions is observed in the core region in the plasma both in DIII-D and NSTX-U as seen in the radial profile of fast ions. In the discharge of NSTX-U, the RSAEs is observed for $t < 400$ms, fishbone is observed for $t = 400 - 500$ ms, and the TAEs/RSAEs is observed for $t > 500$ms. The deviation of neutron rate measured and the kick model from the classical model appears for $t > 400$ms when the fishbone appears and becomes more significant for $t > 500$ms when the TAEs appear. These observations show that the fast ion loss by the TAEs is larger than that by fishbone and RSAEs and the good agreement between the measurements and kick model simulation demonstrates the quite good validation of the model.

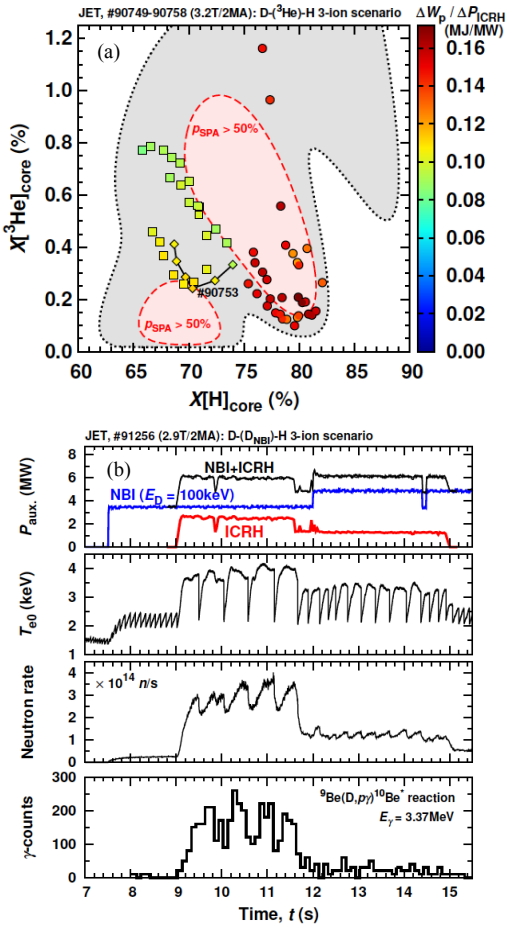

FIG. 12: (a) Increase of the stored energy per ICRF heating power in the parameter space of the ratios of hydrogen and ^{3}He density to electron density for the 3-ion D-(^{3}He)-H scheme at JET. Here, red area is the computed operation regime, where the power fraction by a single-pass absorption, $P_{\rm SPA}$, exceeds 50%. (b) time-traces for NBI and ICRF power, central electron temperature, neutron rate and gamma-ray count rate for the 3-ion D-(DNBI)-H scheme at JET. (Adapted from supplementary information in [20] and figure 2(b) and figure 8(a) in [22]).

E. Heating scenario by ICRF heating and ECRH

A novel heating scenario using Ion Cyclotron Range of Frequencies (ICRF) heating and Electron Cyclotron Resonance Heating (ECRH) has been developed in tokamak and stellarator. A three-ion species ICRH heating scheme

on JET and AUG was reported [19–23]. D-(^{3}He)-H three-ion ICRH scenario (minority heating of ^{3}He ions in H-D plasma) was found to be an efficient technique for heating H-D mixed plasma in JET. As seen in figure 12(a), large increase of stored energy where $\Delta W_p/\Delta P_{ICRH} > 0.15$ MJ/MW is obtained in the plasma with 0.1% - 1 % ^{3}He density and 75% - 82% H density. Note that circles represent pulses in which more than 2MW of ICRH power was coupled with $+\pi/2$ phasing, while squares correspond to pulses in which all RF power was coupled with the dipole phasing. The grey area corresponds to the region, where more than 80% of incoming RF power was computed to be absorbed by ^{3}He minority ions.

Energetic species, such as injected NBI ions and fusion products, can also play the role of the 'third' species. An example of the performance of the three-ion D-(DNBI)-H scenario on JET-ILW with fast D-NBI ions was demonstrated. Figure 12(b) shows an overview of JET pulse #91256 (2.9T/2MA, H-D $\sim$ 85%-15%), where the neutron rate increased by a factor of 10-15 when 2.5MW of ICRH power (f = 25MHz, dipole phasing) was applied simultaneously to 3.5MW of D-NBI. The scenario was tuned such that D-NBI ions with an injection energy of 100 keV absorbed most of the launched ICRH power in the vicinity of the ion-ion hybrid layer and were the case accelerated to much higher energies using ICRH. The presence of a population of energetic D ions with energies $\sim$ 1-2 MeV during the combined ICRH+NBI phase was confirmed by neutron spectroscopy and γ-ray measurements as seen in the bottom panel in figure 12(b).

High density plasma scenario with O2-ECRH and pellet injection was reported from W7-X [24]. As shown in figure 13, the plasma start-up and the first density ramp was performed by 4 ECRH beams in X2-polarization. During the density ramp-up phase of 2 sec the polarization of these beams had been changed from X2-mode to O2-mode and the density was increased by pellet injection to above the X2 cut-off. The second row shows the chance of polarizer position for the 3 "start-up" gyrotron beams, when their polarization was switched from X2 to O2. High densities of up to $n_e(0)$ =1.4 $\times$ 10^{20} m^{-3} were achieved by 141 GHz second harmonic O-mode (cut off density = 2.4 $\times$ 10^{20} m^{-3}) by multiple pellet injections. Although the electron temperature measured with ECE agrees with that measured with Thomson scattering before t = 3.0 sec, ECE signal intensity drops to almost zero as the line-integrated density exceeds the critical value. This is clear evidence that the electron density exceeds the x2-cutoff density (1.2 $\times$ 10^{20} m^{-3}). It was demonstrated that the combination of the switching of the polarization of ECRH from X2-mode to O2-mode and multiple pellet injections was a good scenario to achieve high density ECRH plasma in W7-X.

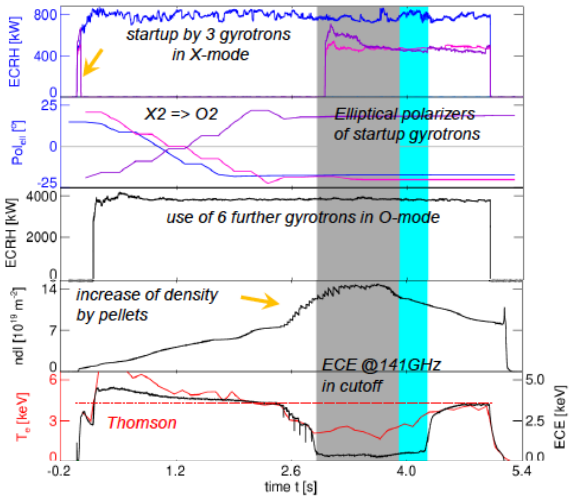

FIG. 13: Time evolution of ECRH power and polarizer position of the 3 "start-up" gyrotron in X-mode, the other ECRH power in O-mode, line-integrated electron density, electron temperature measured with Thomson scattering and ECE, and stray radiation in Wendelstein 7-X. (Adapted from figure 3 in [24]).

III. PLASMA-MATERIAL INTERACTIONS, DIVERTORS, LIMITERS, SCRAPE-OFF LAYER (SOL)

Figure 14 shows physics elements in the field of plasma-material interactions, divertors, limiters and scrape-off layer (SOL). Turbulence spreading from plasma core to SOL and filaments generated at divertor leg has been recognized to play an important role in determining the SOL decay length at divertor plate and hence divertor erosion. Turbulence in SOL is strongly affected by the radial electric field (E_r) shear at the last closed flux surface (LCFS) and the turbulence generated at the pedestal region inside LCFS. The SOL decay length can be controlled by flux expansion, magnetic perturbation, and turbulence in SOL and filaments in divertor leg. Turbulence and filaments also affect the lower-hybrid current drive efficiency.

A. Power decay length in SOL

In the SOL region in tokamak, the power fall-off length is typically small at the mid-plane and this short power fall-off length causes localized heat flux and hence the severe erosion of the divertor plate. The localization of the heat flux at the divertor can be reduced by expanding the

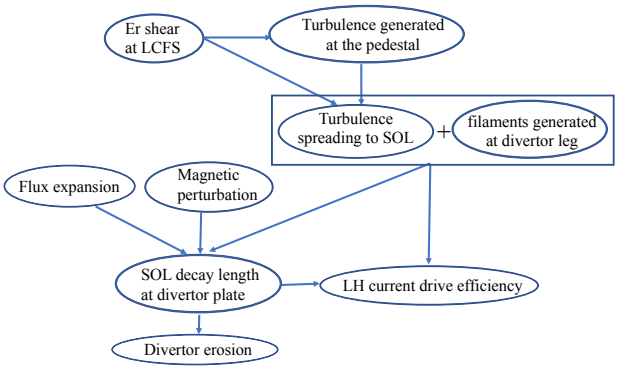

FIG. 14: Diagram of physics element in the field of plasma-material interactions, divertors, limiters, scrape-off layer (SOL)

magnetic flux surface, which is called flux expansion. In order to distinguish the geometric change due to the flux expansion and change in SOL transport, the upstream-remapped power decay length (λ_q) is evaluated.

Results of flux expansion experiment were reported from TCV. Figure 15 shows the ratio of power fluxes to inner and outer-divertor targets, SOL power decay length, and spreading factor, which describes the transport scale length in the divertor SOL, as a function of flux expansion f_x [25, 26]. Here, the flux expansion is defined as $f_x = (B_p/B_{tot})_{MP}(B_p/B_{tot})^{-1}_{SP}$, where MP, SP and B_p is the poloidal magnetic field, and B_{tot} is the total magnetic field, both evaluated at the mid-plane separatrix (R_{MP}) and at the strike point (R_{SP}). Both an increase in divertor-leg length and in flux expansion has the effect of reducing the asymmetry in power load at the inner and outer targets. Their ratio increases to nearly unity at the largest values of flux expansion. However, the increase of the connection length by flux expansion has a much weaker effect on power decay length. Although the spreading factor at the inner target plate is almost unchanged in the wide range of flux expansion, the spreading factor at the outer target plate decreases almost proportional to the inverse of flux expansion as $S_u \propto f_x^{-0.97}$. This variation is attributed to a decrease in the outer conductance.

The dynamic control of heat flux profile at the divertor target plate using the perturbation magnetic field of RMP was reported from DIII-D [27, 28] and KSTAR [29]. Figure 16 (a) shows measured heat flux profiles during pure n=3 RMP, and additional $n = 2$ RMP with a phase at $\phi = 0°$ and $\phi = 180°$ in DIII-D. Prominent heat flux splitting on the outer divertor has been observed using the IR camera during ELM suppression by n=3 RMP in this low collisionality regime. Variation of heat flux splitting pattern of different $n = 2$ phases in

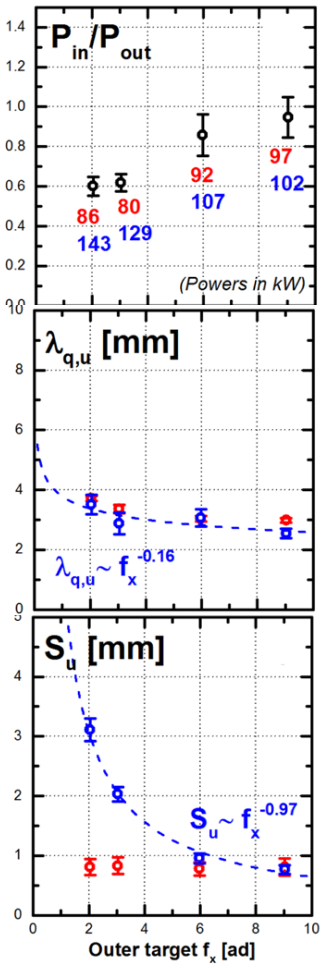

FIG. 15: Ratio of power fluxes to inner (red) and outer (blue) target plates (P_{in}/P_{out}), SOL power decay length (λ_q), spreading factor (S_u) as a function of flux expansion of f_x in TCV. (Adapted from figure 5(g)(h)(i) in [26]).

these mixed toroidal harmonic cases are observed. These characteristics agree well with modeling of field penetration depth using TOP2D with plasma response modeled by MARS-F. Similar experimental observation is also reported in KSTAR. Figure 16 (a) shows the radial profile of heat flux in the plasma with 3-row $n = 1$ RMP with a phasing of (-90°, 90°), (-85°, 85°), (-80°, 80°), and (-75°, 75°) in KSTAR. The radial profile of heat flux with RMP is broader than that without RMP. Variation of the heat flux pattern at different phasing is also reported in KSTAR.

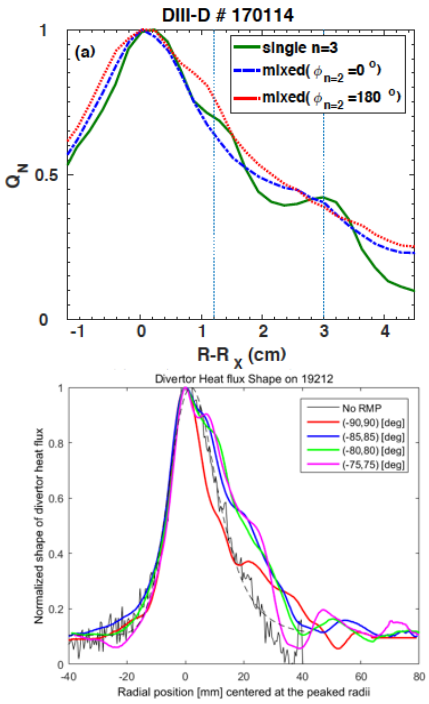

FIG. 16: (a) Radial profile of heat flux in the plasma with n=3 RMP and $n = 2$ RMP with a phase at $\phi = 0°$ and $\phi = 180°$ in DIII-D, and (b) radial profile of heat flux in the plasma with 3-row $n = 1$ RMP with a phasing of (-90°, 90°), (-85°, 85°), (-80°, 80°), and (-75°, 75°) in KSTAR. Here the heat flux is normalized with a peak value. (Adapted from figure 4(a) figure 6(a) in [28] and figure 6 in [29]).

Turbulence in SOL and filaments in divertor leg are expected to contribute to broadening of the radial profile of heat flux and increase of power decay length. The measurements of the fall-off length of power, density and temperature during L-mode, I-mode and H-mode transition were reported from ASDEX Upgrade tokamak [30, 31]. The fall-off lengths of power both in the outer and the inner divertor decrease after the transition from L-mode to I-mode phase and a further decrease is observed after the transition to H-mode. As seen in the change in the fall-off length of the density and temperature, the decrease of the power fall-off length at the transition from L-mode to I-mode is mainly due to the decrease of the fall-off length of temperature (λ_T). In contrast, the decrease of the power fall-off length at the transition to H-mode is mainly due to the decrease of fall-off length of density (λ_n). These observations suggest that suppression of temperature fluctuation in I-mode causes the decrease of λ_T and λ_q and the suppression of the density

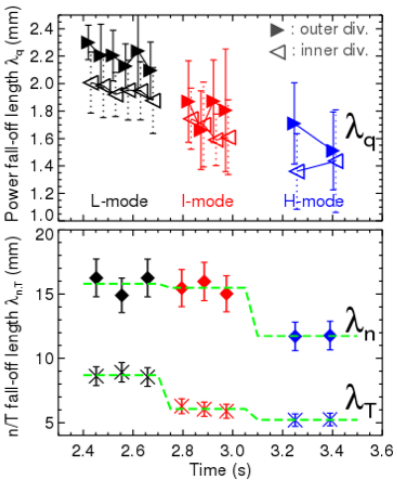

FIG. 17: (a) Power fall-off length (λ_q) mapped to the outer midplane and (b) corresponding SOL density fall-off length (λ_n) and temperature fall-off length (λ_T) during L-mode, I-mode and H-mode transition on ASDEX Upgrade tokamak. (Adapted from figure 4(e)(f) in [31]).

fluctuation in H-mode causes the decrease of λ_n and λ_q.

B. Turbulence/filaments and flow in the SOL and divertor leg

In the transport study, the spreading turbulence is usually ignored and the turbulence observed is assumed to be locally driven. However, in the region where the pressure gradient is small, such as inside magnetic island and SOL, the spreading turbulence can be dominant. In fact, experimental data suggesting the spreading turbulence have been reported in magnetic island and SOL. Turbulence spreading into the O-point from the X-point of the magnetic was experimentally identified from the hysteresis relation between temperature and turbulence in the heat pulse propagation experiment in DIII-D [32].

In the SOL, turbulence which is spreading from the plasma inside LCFS could be important, because the locally driven turbulence is relatively weak in the SOL region where the temperature and density gradients are small. The novel analysis of turbulence to distinguish the origin of the turbulence with the modulation of bias was reported from TJ-II [33]. In this analysis, the rate of turbulence drive and the rate of turbulence spreading are defined as $\omega_D = -2\langle\partial n/\partial r\rangle\langle\tilde{V}_r\tilde{n}\rangle/\langle\tilde{n}^2\rangle$ and $\omega_S = \partial\langle\tilde{V}_r\tilde{n}^2\rangle/\partial r/\langle\tilde{n}^2\rangle$. The angular brackets $\langle ...\rangle$ indicates a running average over a time interval much larger than the turbulence correlation time. The impact of edge-biasing on the local turbulence drive (ω_D) and the tur-

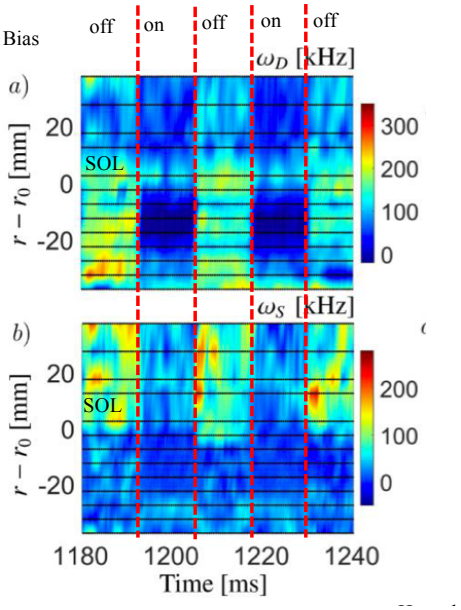

FIG. 18: Contour of rate of turbulence drive (ω_D) and turbulence spreading (ω_S) in time and space with modulation of limiter bias in TJ-II. (Adapted from figure 5(a)(b) in [33]).

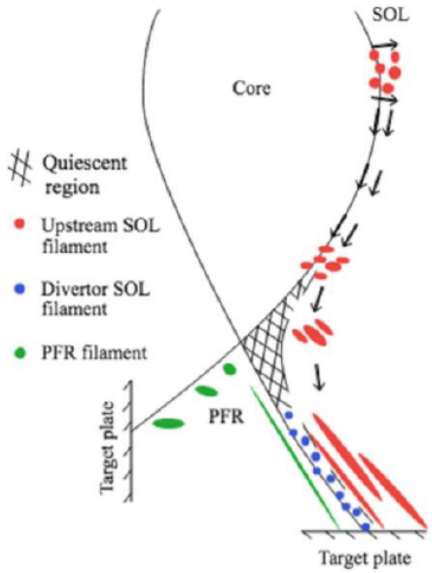

FIG. 19: Schematic of the different contributions to intermittent cross-field transport in the divertor observed in MAST. (Adapted from figure 6 in [34]).

bulence spreading (ω_S) can be seen in figure 18. When the bias is turned on, locally driven turbulence inside LCFS ($r - r_0 < 0$) is substantially reduced due to the edge radial electric field shear. The impact of edge radial electric field shear on the locally driven turbulence outside LCFS ($r - r_0 > 0$) is small. In contrast, spreading turbulence inside LCFS ($r - r_0 < 0$) is almost unchanged during the bias modulation. Spreading turbulence outside LCFS ($r - r_0 > 0$) is significantly reduced due to the edge radial electric field shear. Thus, when the shear of the ExB flow reaches a value comparable to the inverse of the turbulence correlation time, the level of turbulence spreading is affected and, as a consequence, the level of edge-SOL coupling also is affected. Therefore, the shearing rate of edge radial electric fields may be an important tool to suppress turbulence and also to decouple the edge and SOL regions, since it reduces the level of non local effects (turbulence spreading).

Recent development of high speed camera reveals the turbulence and filament structure in the SOL region and divertor keg. Observation of filaments at the SOL and divertor-leg was recorded from MAST. Several regions where the characteristics of the observed filaments are qualitatively different are observed using the high-speed imaging of the lower divertor in MAST [34, 35] as seen in figure 19. High frequency filaments with a small size ($\sim$ 1cm) are observed close to the separatrix of the outer leg away from the X-point and in the private flux region Filaments generated upstream (red) are shared by the X-point and aligned along the magnetic field at the divertor leg near the target plate. In contrast, the filaments locally generated (blue) at the divertor leg are not field aligned. Filaments at the private flux region (green) are small high frequency filaments.

Another observation of filaments at the SOL and divertor-leg was reported from NSTX-U. In the NSTX-U, image of C III emission are measured using high speed imaging camera with 9 μs exposure [36, 37]. The typical structure of divertor filaments is shown in 20(a) with a rendering of flux tubes in the NSTX-U divertor corresponding to divertor localized fluctuations. Figure 20(b) shows filaments on the inner and outer divertor legs with an image of the lower divertor. Filaments were approximately field aligned, connected to the divertor target plate and localized to the bad curvature region on both the inner (i.e., in the private flux region) and the outer-divertor legs (i.e., in the common flux region). Measurements of poloidal and radial correlation length using high speed imaging camera suggest the local generation of filaments. The experimental observations with a high speed camera reveal that the complexity of the turbulence structure in the SOL region. The filament generated at the upstream SOL (mid-plane) and the filament generated at divertor leg co-exist in the divertor leg. Al-

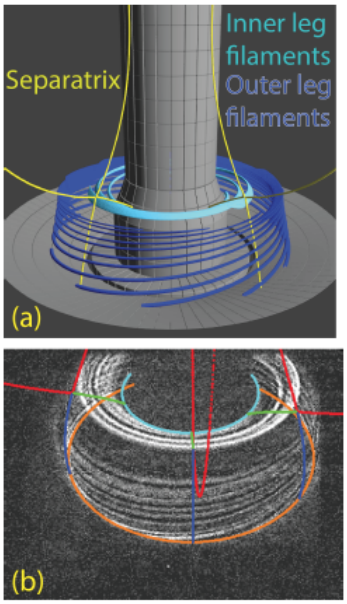

FIG. 20: (a) Rendering of the NSTX-U divertor with flux tubes corresponding to divertor-localized fluctuations; (b) Divertor image in C III emission (9 μs exposure) after high pass filtering. Separatrix (red), inner (green) and outer (blue) divertor legs, inner (cyan) and outer (orange) strike points are overlaid. (Adapted from figure 1(b) and figure 4(d) in [36]).

though the filament generated at the upstream SOL is expected to be elongated along the magnetic field (field aligned), the filament locally generated at divertor leg has a small structure. The enhancement of turbulence and filaments of SOL and divertor leg provies another knob to control the power decay length.

The measurements of parallel flow velocity were reported from DIII-D and LHD. The structure of the plasma flow parallel to the magnetic field is measured by the Doppler shift of the impurity emission in the SOL and divertor region in order to identify the parallel convective transport towards the target plate. The coherence Imaging Spectroscopy (CIS) diagnostic [38] provides a tangential image of the CIII intensity (465nm) and flow velocity along the line-of-sight. Figure 21 shows the image of tangential views of C^{2+} flow that have been inverted onto the poloidal plane in the density where the C^{2+} velocity is well coupled to the background deuterium velocity [39]. The flow images suggest a parallel flow towards the target throughout the divertor in the range of 15 -30 km/s. Flow towards the outboard target plate is observed in the wide region near the outer leg, while the parallel flow towards the inboard is observed in the private region. These flow velocities are roughly equal to

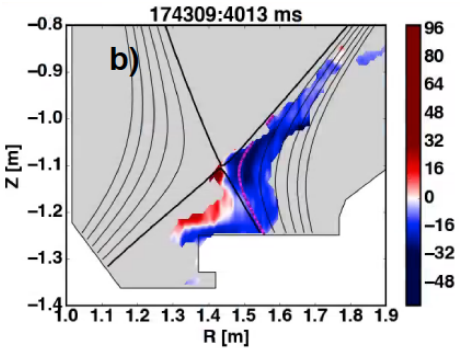

FIG. 21: Image of toroidal (parallel) flow of carbon impurity (C^{2+}) measured from the Doppler shift of CIII emission using Coherence Imaging Spectroscopy (CIS) in DIII-D. Negative flow velocity (blue) is toward the divertor target. (Adapted from figure 10(b) in [39] (figure 8(b) in [14])).

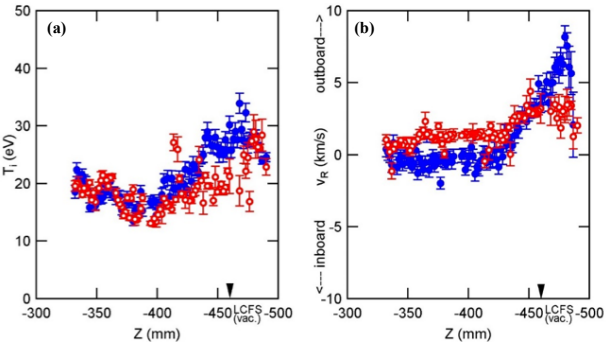

FIG. 22: Vertical profiles at the bottom edge of the ergodic layer of (a) ion temperature, and (b) flow velocity derived from the Doppler profile of the second order of CIV line emission (2 × 154.82 nm) for inward shifted magnetic configuration with R_{ax} = 3.6 m in LHD. Open and closed circles show the results from D plasma (red) and H plasma (blue), respectively. (Adapted from figure 5 in [40]).

the ion sound speed for $T \sim$ 3-5 eV characteristic of the divertor plasma. Imaging of plasma flow implies parallel plasma flow towards the target in the divertor near the sound speed, $M \sim 1$.

Figure 22 shows vertical profiles at the bottom edge of the ergodic layer of ion temperature, and flow velocity derived from the Doppler profile of the second order of CIV line emission in LHD [40]. The measured flow velocity (v_R) is the projection of the flow along the observation

chord which can be approximately considered to be the direction of the plasma major radius. Assuming that the flow measured is simply the projection of flow parallel to the magnetic-field lines to the line-of-sight of the measurements, the value of parallel flow can be evaluated by $v_{\parallel} = (B_{\phi}/B_R)v_R$ The flow velocity toward the outboard direction develops clearly with the maximum value at Z = -480 mm, which is a location close to the outermost region of the ergodic layer in the H plasma. The location of the LCFS is Z = -460 mm and the peak of the flow velocity is located 20mm outside the LCFS. The ion temperature has no clear change between the H plasma and the D plasma, and $\sim$ 30 eV at the peak of plasma flow. Flow velocity of v_R is larger (11.3 km/s) for H plasma than that (8.0 km/s) for D plasma. The difference of the estimated values between D and H plasma is caused by $m_i^{1/2}$ dependence of parallel velocity when the friction force term is dominant in the force balance. In LHD, the parallel plasma flow towards the outboard divertor target plate at the upstream of SOL is one-half of the sound speed, $M \sim 0.5$. The Doppler shift measurements with impurity emission in DIII-D and LHD confirm that the parallel plasma flow in the SOL and divertor leg is towards the divertor target plate and near ion sound velocity (mach number of the parallel flow velocity is 0.5 $\sim$ 1).

C. Impact of SOL turbulence on LH current drive efficiency

The novel measurements of LH electric field vector were reported from Alcator C-Mod. The LH electric field vector, E_{LH}, was directly measured in the edge region of Alcator C-Mod using dynamic Stark spectroscopy (DSS) by fitting the Schrodinger equation to the shape of π and σ polarized spectra of D_β simultaneously [41, 42]. Figure 21(a) shows the example of π and σ polarized spectra of D_β with fitted lines by Schrodinger equation where the magnitude of E_{LH} is fitting parameters. Experimentally, E_{LH} was found to be composed of nearly equal poloidal and radial components. In the simulation, E_{LH} was found to be nearly radial. Figure 21(b) shows the direction of E_{LH} averaged over LH power as a function of vertical locations. The direction of E_{LH} is nearly 70° - 80° in the simulation without density fluctuation. When the density fluctuation is added into the simulation, the direction of E_{LH} becomes 40° - 50°, which is much more consistent with the direction measured with DSS. This results indicates that SOL density fluctuations cause severe scattering of the LH wave in $k_\perp$ space and make the magnitude of the poloidal component equal to that of the radial component. It is concluded that diffraction and scattering by turbulence driven scrape off layer density fluctuations is the responsible mechanism behind the experimentally observed modification in the direction of E_{LH}. These results further support the proposition that edge turbulence is an important mechanism behind

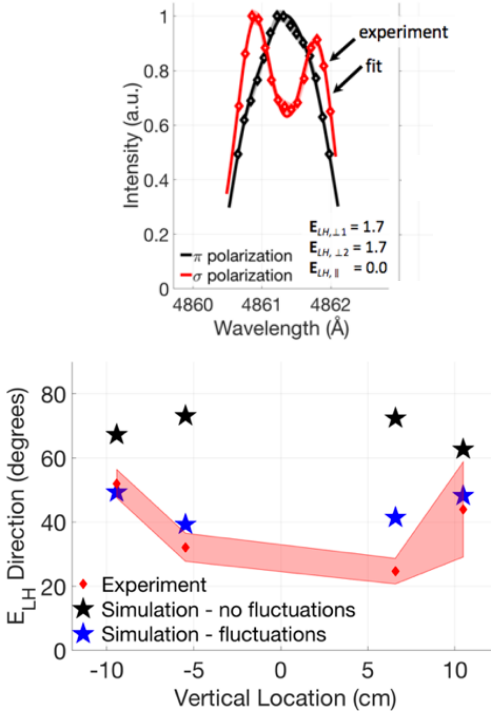

FIG. 23: (a) Experimental (markers) and fit (line) π and σ polarized spectra and (b) Direction of E_{LH} averaged over LH power as a function of vertical locations in Alcator C-mod. (Adapted from figures 4 in [42] and figure 7 in [41]).

the anomalous drop in LH current drive efficiency for diverted plasma in the high density regime.

Efficient lower hybrid current drive (LHCD) at densities up to $\bar{n}_e \sim 1.5 \times 10^{20}$ m^{-3} was demonstrated in the Alcator C-Mod tokamak. Figure 24 summarizes the non-thermal bremsstrahlung emission rates as a function of line-averaged density [43, 44]. At fixed line-averaged density, the count rates measured at low Greenwald fractions (I_p = 1.2 and 1.4 MA) are increased by more than two orders of magnitude compared to those at the lowest current (0.55 MA). This result suggests that a recovery of efficient LHCD correlates with the change in the edge/SOL density condition, rather than on the temperature. The recovery of current drive efficiency to a level consistent with engineering scalings is related to a reduction in density shoulders and turbulence levels in the far SOL. The experiment in Alcator C-Mod demonstrated that the density fluctuations in SOL are an important parameter in determining the LH current drive efficiency

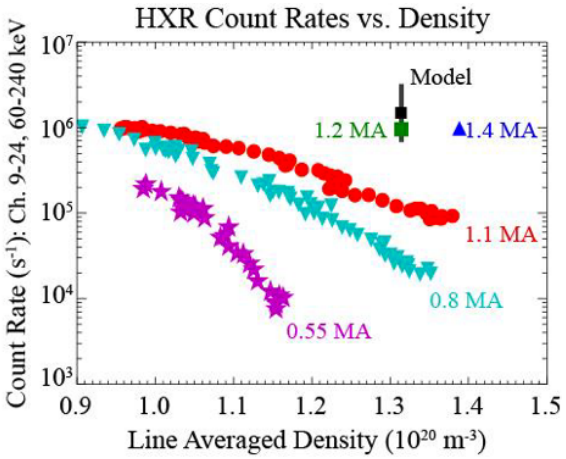

FIG. 24: (a) The line-integrated hard X-ray count rates as a function of the line-averaged density at different plasma currents: 0.55 MA (star), 0.8 MA (upside-down triangle), 1.1 MA (circle), 1.2 MA (square), and 1.4 MA (triangle) in Alcator C-mod. The hard X-ray rates are normalized to the square root of the input power. (Adapted from figure 3 in [43]).

because it causes severe scattering of the LH wave and changes the direction of LH electric field vector. The reduction of SOL density fluctuation is desirable for high LH current density efficiency in a high density plasma. This feature is compatible with the requirement for the long power decay length in SOL, because the enhancement of SOL density fluctuation is preferable to increase the power decay length in SOL and to reduce the heat load on the divertor plate.

D. Detachment

Detachment experiments have been investigated as another approach to reduce the heat load on the divertor plate. Long pulse discharge was demonstrated in the Wendelstein 7-X (W7-X) stellarator with magnetic island divertor in the detached condition [45–47]. As seen in figure 25, the transition to detachment occurred at $t =$ 2 sec during a density ramp with the heating power held approximately constant around 2.7 MW, and detachment lasted until the programmed end of the discharge at $t =$ 4 s. A local heat flux to the divertor target is reduced by about one order of magnitude during detachment. The detached condition was also applied to demonstrate the long pulse discharge over 30 sec with the central electron density of $n_e \sim 8 \times 10^{19}$, central electron temperature of 2.4keV and the global energy confinement time of 125 ms.

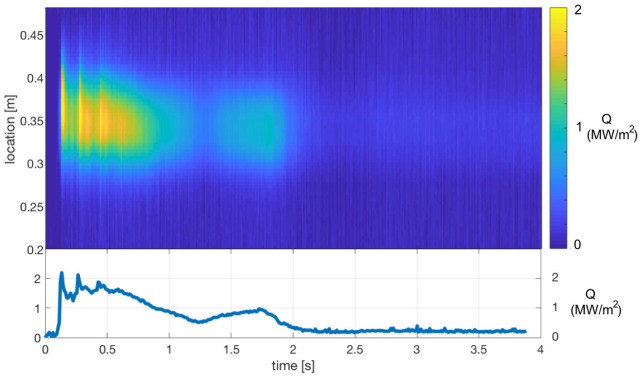

FIG. 25: Infrared camera data and time evolution of the local heat flux at the divertor target in Wendelstein 7-X long pulse discharge. (Adapted from figure 4 in [45]).

Effects of magnetic island produced by a resonant magnetic perturbation (RMP) field at the plasma edge on detachment was reported in LHD. In helical plasma, the electron density is limited by the radiation collapse because there is no disruption in high density. Density limit, $n_{\rm sudo}$ was found to be determined as $0.25PB/a^2/R)^{0.5}$, where P, B, a and R are heating power (MW), magnetic field (T), minor radius (m) and major radius (m), respectively. As seen in figure 26, the radiation increases sharply as the plasma density is approaching the critical density so-called Sudo density limit, $n_{\rm sudo}$ in the plasma without RMP field [48]. In this experiment, the heating power is 7 - 8 MW and the density limit $n_{\rm sudo}$ is $\bar{n}_e \sim 9 \times 10^{19}$ with the energy confinement time of 50 ms. However, when the RMP field is applied, the plasma shows the transition from attached phase to detached phase at the density much below the Sudo density limit, $\bar{n}_e/n_{\rm sudo} \sim 0.45$. After the detachment, the increase of radiation power is gradually increased even near the Sudo density limit. Therefore, the magnetic island produced by the RMP field enhances the transition to the detachment phase and results in the access to the higher density. It was found that the RMP application leads to easier control of detached plasma in LHD. The detached experiment in W7-X and LHD demonstrated that the magnetic islands near the plasma boundary are quite beneficial to control the detached plasma and access to the steady-state long pulse operation with high density.

The transition from attached condition to strongly detached condition at the high density was demonstrated in tokamaks. As seen in figure 27(a), the electron temperature measured with divertor Thomson scattering in front of the low field side (LFS) of target plate shows the abrupt drop when the upstream separatrix electron den-

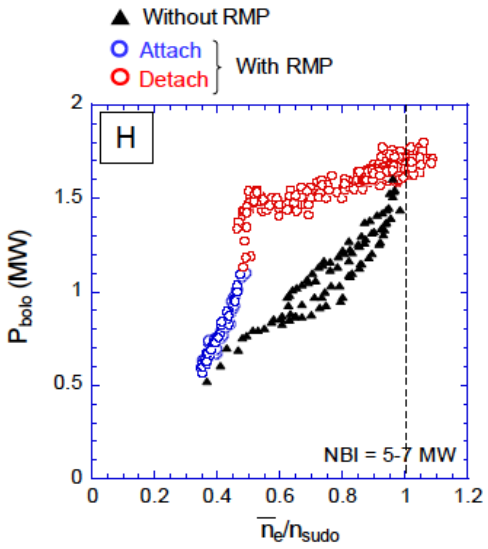

FIG. 26: Radiated power measured with bolometer in toroidal section #3, as a function of density normalized with Sudo density limit in LHD. Black triangles: without RMP; blue circles: attached with RMP; red circles: detached with RMP. The data of NBI heating power 5 to 7 MW are plotted. Hydrogen plasma. (Adapted from figure 3 in [48]).

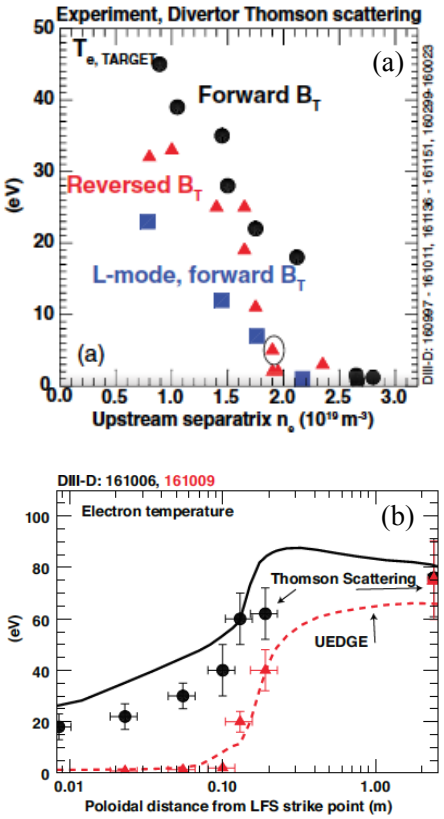

FIG. 27: (a) Measured electron temperature in front of the low field side (LFS) target plate as a function of measured electron density at the separatrix in the main SOL in high confinement mode plasmas and (b) measured (symbols) and simulated (line) electron temperature along a flux tube in the LFS SOL in DIII-D. Black symbols and line are an attached case, red is a detached case. (Adapted from figure 4(a) in [49] and figure 3(a) in [50]).

sity exceeds a critical value [49, 50]. The critical value depends on the direction of magnetic field. The critical density is higher in the case of forward B_T (∇B-drift towards the X-point and lower power threshold for H-mode) than in the case of reversed B_T (∇B-drift away from the X-point and higher power threshold for H-mode). Figure 27(b) shows the comparison of measured electron temperature along a flux tube in the LFS SOL to that predicted by UEDGE simulation code in the attached condition (black) and detached condition (red). The UEDGE simulation includes full cross-field drift and SOL current and reproduces the experimentally observed step-like inset of LFS divertor detachment with increasing plasma density in the case of forward B_T. Discharges with SAS divertor also show less degradation in H-mode confinement factor with increasing edge pedestal density than that with open LSN divertor or more closed USN divertor for similar conditions.

New concept of divertor was reported from DIII-D. A prototype Small Angle Slot (SAS) divertor, which consists of progressive opening and small angle target, has been installed on DIII-D as illustrated in figure 28(a) [14]. SAS was designed to both enhance neutral trapping and optimize neutral distribution along the target to achieve strong plasma cooling across the divertor at a lower upstream plasma density [51]. As seen in figure 28(b), the critical density for the transition from attached condition to detached condition indicated by the abrupt drop of electron temperature is $\bar{n}_e/n_G = 0.37$ for SAS divertor, which is lower than that ($\bar{n}_e/n_G = 0.5$) for the conventional divertor (closed upper single null divertor).

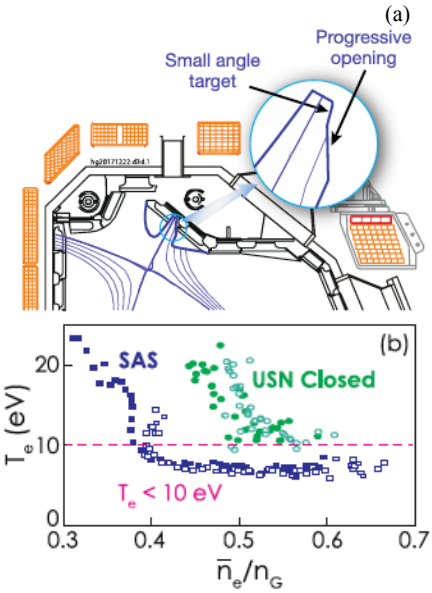

FIG. 28: Prototype Small Angle Slot (SAS) divertor and comparison of electron temperature near strike point as a function of electron density normalized by Greenwald density for SAS (blue), open lower divertor (red), and more closed upper divertor (green) in DIII-D. (Adapted from figure 13 and figure 14(b) in [14]).

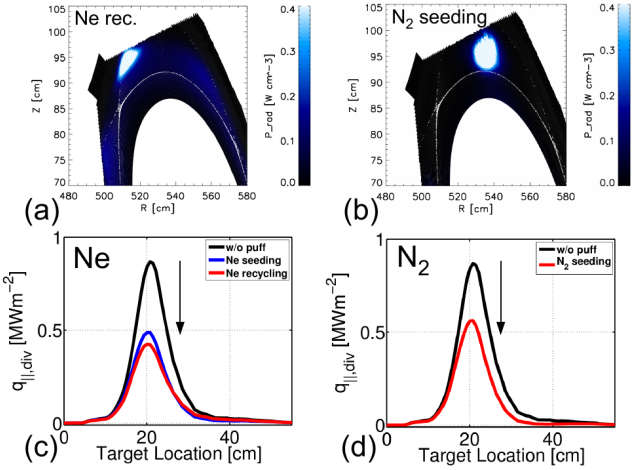

FIG. 29: Total P_{rad} of Ne after puff sourced proportional to recycling flux (b) total P_{rad} of N2 during puff neglecting recycling (c) averaged divertor heat fluxes for Ne with (red) and without recycling (blue) (d) averaged divertor heat fluxes in case of N2 seeding without recycling in Wendelstein 7-X. (Adapted from figure 4 in [54]).

1. *Impurity seeding*

The 3D coupled plasma fluid and kinetic neutral edge transport Monte Carlo code EMC3-EIRENE is commonly used for predictive modeling and the interpretation of experimental results in the domain of plasma wall interactions and SOL transport [52, 53]. Calculations of EMC3-EIRENE for the first attempt in preparation of seeding experiments were reported from Wendelstein 7-X [54, 55]. Impurity seeding in the island divertor was simulated either assuming sourcing scaled with the main recycling flux or sourced from the puff location only. Figure 29 shows the main results of a first comparison of the features of radiative power exhaust with neon (Ne) and nitrogen (N2) seeding within the modeling and its impact on divertor heat flux. Significant reduction of heat flux on the target plate is predicted both for Ne and N2 seeding. In the case of Ne seeding, the impact of recycling on the reduction of heat flux is studied. The heat fluxes are slightly less reduced in the case of Ne sourced from the puff location in the island center without recycling. By including the recycling effect, further reduction of heat flux due to impurity seeding is predicted. 3D modeling using EMC3-EIRENE confirms the main features of the power exhaust experiments in Wendelstein 7-X.

The effect of magnetic geometry on scrape-off layer (SOL) transport and detachment behaviour was also reported from TCV [25, 56]. As seen in figure 30, a significant reduction of ion saturation current j_{sat} at the outer target in the vicinity of the separatrix (ρ_φ=1) is observed with nitrogen seeding. The strong peak at the separatrix observed before the nitrogen seeding vanishes after the nitrogen seeding, which is a clear indication of the partial detachment. After the nitrogen seeding, j_{sat} profile shows small double peaks across the separatrix. Edge transport simulation in TCV shows that divertor dynamics are modified by the existence of significant $E \times B$ drifts. The $E \times B$ drifts are one of the candidates for splitting of the heat flux during the nitrogen seeding. The simulation including $E \times B$ drifts predict the double peaked heat flux profile at the inner strike point in TCV [57]. However, the double peaked heat flux profile is not predicted in the simulation with impurity seeding experiment in Wendelstein 7-X.

The impurity seeding experiment demonstrates a significant reduction of heat flux on the target plate, which can reduce the erosion of the divertor plate significantly. The impact of impurity seeding is not just the decrease of the magnitude of the heat flux. Heat flux profile is modified by impurity seeding as seen in the splitting of

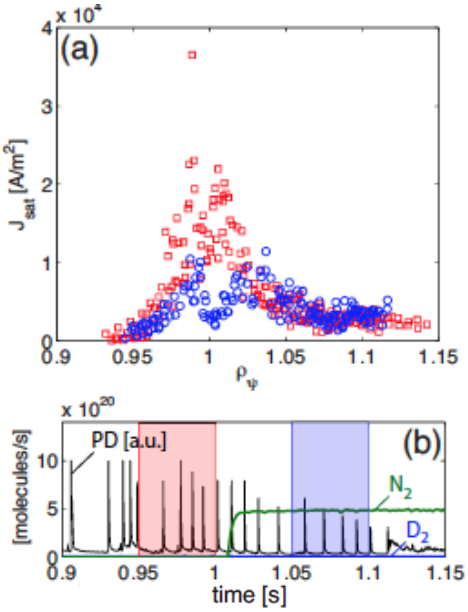

FIG. 30: (a) Profile of the ion saturation current of Langmuir probe (LP) at the outer target inter-ELM during the intervals before (red) and after (blue) the start of the nitrogen seeding and (b) by the time evolution of D_α photodiode (PD) signal in TCV. (Adapted from figure 8(a)(b) in [25]).

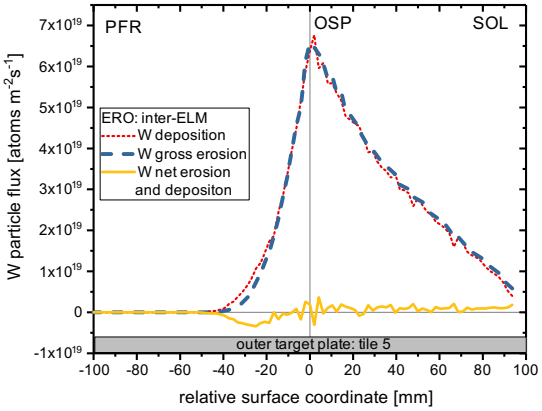

FIG. 31: Tungsten (W) particle flux as a function of relative surface coordinate in JET. (Adapted from figure 4(b) in [59]).

the sharp peak of heat flux to small two peaks at the separatrix. Impurity seeding can be a candidate to the mitigation of the localized heat flux at the target plate in the H-mode plasma, where the power decay length at SOL is shortest due to the reduction of turbulence in SOL as discussed in the previous section.

E. Erosion and sputtering

Detailed analysis of tungsten erosion and sputtering was reported from JET. The outer strike point (OSP) was located on a part of the bulk-W divertor (tile 5, stack C) which could be correlated to the exposure in this period of plasma operation before tile removal. The electron temperature and density at OSP are 35eV and $6 \times 10^{19}\mathrm{m}^{-3}$, respectively. A comparison of W source spectroscopy in the intra- and inter-ELM phases with the post-mortem analysis provides a pair of gross and net W erosion. W gross erosion determined by the optical emission spectroscopy (OES) is 40 - 60g. In contrast, net erosion determined by the post-mortem analysis (PMA) of deposition of the divertor tile after the removal is 2.4 - 4.8g over the 900s considering the interaction are in the circumference of the outer divertor. This corresponds to a higher-deposition fraction of more than 94 % averaged over both phases. The plasma-material interaction and transport code (ERO) coupled with improved PIC modelling for the complex re-deposition in both phases was applied to simulate a comparable experimental case [58]. Figure 31 shows the erosion and deposition distribution along the outer target plate in the conditions at the OSP. The ERO code can reproduce the large gross erosion, the low net erosion, and thus the local high re-deposition on tile 5 with more than 94% in average and at 99% for the sputtering dominating intra-ELM phase [59].

The erosion of tungsten (W) by plasma isotope species (H, D and T) and intrinsic impurity (Be) and extrinsic impurity (N, Ne or Ar) sputtering determines both the lifetime of divertor components and the impact on plasma performance. Binary collision approximation SDTrimSP simulations [60] allow predicting the potential isotope dependences for the physical sputtering and thus give an insight into how sputtering may impact the integration of the main DT scenarios with the W/Be wall. Figure 32 shows the sputtering yields of both Be and W by bulk ions (H,D, and T) as a function of impact energy which is strongly dependent on the plasma conditions, such as L-mode, Inter-ELM, hybrid scenario and intra-ELM [23]. The sputtering yields of Be has a peak at $\sim$ 100 eV which corresponds to the plasma condition for Inter-ELM and hybrid scenario. In this energy range, the sputtering yields of W are negligible. Sputtering yields of W start to increase when the incident ion energy exceeds a few hundred eV and become significant above 1 keV, which corresponds to the plasma condition for intra-ELM. The isotope effect on the sputtering yields is clearly observed. The sputtering yields of Be by T and by D are 2.5 and 2

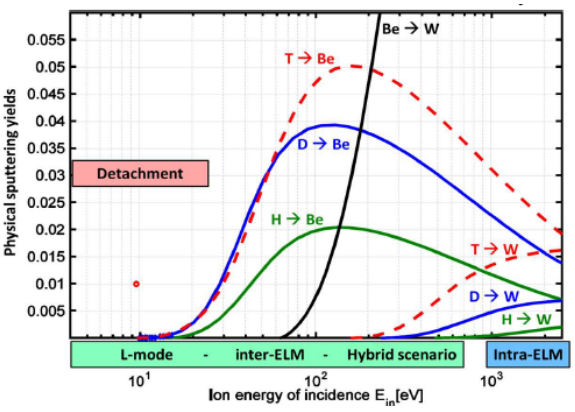

FIG. 32: Isotope (H: green, D:blue, T:red) effect on the Be and W sputtering yields simulated by the code SDTrimSP in JET. W sputtering yield by Be is also shown in black. (Adapted from figure 12 in [23]).

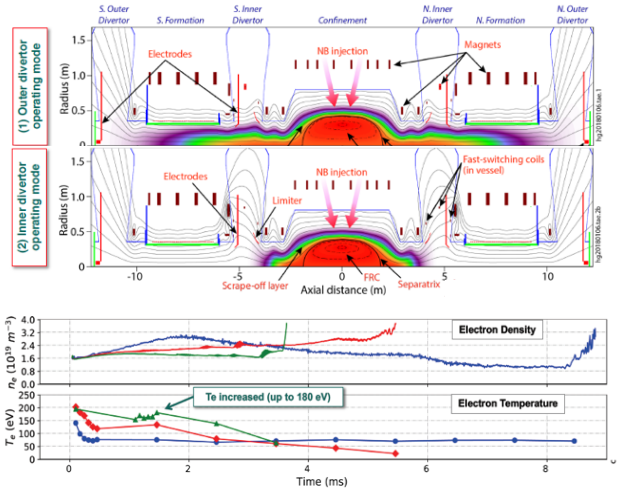

FIG. 33: Sketches of FRC magnetic topology and density contours, simulated by the 2-D MHD LamyRidge equilibrium code, in (a) outer-divertor operating mode and (b) inner-divertor operating mode with flared magnetic-field, and (c) time evolution of electron density and temperature in the plasma discharges under three different machine configurations without inner-divertor magnetic field flaring with outer-divertor edge-biasing (blue), with field flaring but without edge-biasing at all (red), and with field flaring and outer-divertor biasing (green) in C-2W. (Adapted from figure 1(b)(c) and figure 10 in [61]).

times the sputtering yields by H. In contrast, the sputtering yields of W by D and T are 5 - 10 times that of H in the energy range for intra-ELM. This simulation implies that the erosion of W during intra-ELM will be serious problems in the D-T mixture plasma in future.

IV. INNOVATIVE CONFINEMENT CONCEPTS

Experimental results of the newly constructed C-2W experimental device (also called "Norman") were reported. It is the world's largest compact-toroid (CT) device, which has several key upgrades from the preceding C-2U device such as higher input power and longer pulse duration of the NBI system as well as installation of inner divertors with upgraded electrode biasing systems. Figure 33(a)(b) shows FRC magnetic topology and density contours for two operation modes [61]. One mode is the outer-divertor operating mode and the other mode is the inner-divertor operating mode. Figure 33 shows the typical plasma discharges under three different machine configurations. One discharge is without inner-divertor magnetic field flaring with outer-divertor edge-biasing, which is a C-2U-like configuration. In this configuration, plasma was sustained for more than 8 ms. The other configuration is that with field flaring but without edge biasing at all. The plasma was sustained for ~ 6 ms. The last configuration is that with field flaring and outer-divertor biasing. Although the duration of the plasma discharge is only ~ 4 ms, the highest electron temperature ($150 \sim 200$ eV) was obtained.

The experimental results of high-power reconnection heating of ST plasma in TS-3, TS-4 and MAST were reported. The reconnection heating has been recognized to be efficient enough to realize a significant increase of ion temperature as the reconnecting magnetic field B_{rec} increases. As shown in Figure 34, when the two STs are merged an X-point is formed at their contacting point and finally a new high-beta ST [62]. The increase of the ion temperature (ΔT_i) due to the reconnection heating is proportional to reconnecting magnetic field B_{rec}^2 as seen in the database of merging experiments in TS-3, TS-4 and MAST in figure 34(c). Here the electron density is $n_e \sim 1.5 \times 10^{19}$ m^{-3}. Although the increase of ion temperature is in the range of 10 - 100 eV in TS-3, it was extended to 1.2 keV in MAST.

Although the plasma parameter obtained in the experiment of innovative confinement concepts is far from the parameters required for the fusion reaction, the heating mechanism using the magnetic field is interesting and the knowledge obtained in these experiments can contribute to deep understanding in the heating mechanisms of solar flare.

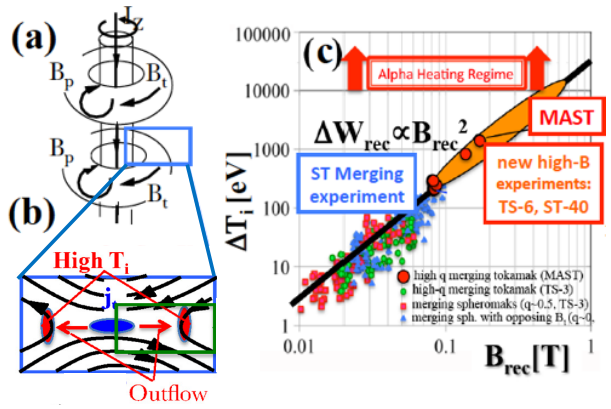

FIG. 34: (a) Two merging ST plasmas and (b) expanded view of X-point region, and (c) dependence of ion temperature increment ΔT_i on reconnecting magnetic field B_{rec} of merging STs and spheromaks under constant electron density $n_e \sim 1.5 \times 10^{19}\mathrm{m}^{-3}$. (Adapted figure 2 in figure 5(a) in [62]).

V. CONCLUDING REMARKS

Interesting results on the coupling between energetic particle, MHD, wave-particle interaction, turbulence, SOL physics, and divertor are presented in this conference. Although EP-driven instability has little impact on bulk confinement, it has significant impact on fast ion confinement and hence causes the degradation of heating efficiency. The suppression of EP-driven instability by ECH or RMP has been demonstrated in several tokamaks (ASDEX Upgrade, HL-2A, KSTAR) and the helical system (LHD, Heliotron-J). Energetic particle transport simulation has been developed and validated with energetic particle diagnostics (neutron rate and FIDA signal) in DIII-D and NSTX-U. Novel heating scenarios using Ion Cyclotron Range of Frequencies (ICRF) heating and Electron Cyclotron Resonance Heating (ECRH) have been developed in tokamak and stellarator. ICRF using three-ion species has been developed in JET, Alcator C-Mod and AUG and dynamic control of polarization of ECRH was developed to achieve high density in Wedenlstein 7-X.

In the tokamak with high magnetic field such as ITER, the power decay length in SOL is predicted to be short and to cause severe erosion at the divertor plate due to the highly localized heat flux at the strike point at the separatrix. Several approaches to control the power decay length have been developed. The flux expansion was found to be inefficient for increasing the upstream power decay length in TCV. The modification of the heat flux profile of RMP has been demonstrated in DIII-D, EAST, and KSTAR. It is found in ASDEX that the power decay length becomes shorter in the H-mode plasma than in the L-mode plasma. This is speculated to be due to the reduction of turbulence in SOL associated with the suppression of turbulence spreading observed in TJ-II. The complicated structure of turbulence, filaments and plasma flow in the SOL and divertor leg has been investigated using imaging measurements recently developed in MAST, NSTX-U, DIII-D and LHD. Although turbulence in SOL is beneficial for increasing the power decay length, turbulence reduces the LHCD efficiency due to the scattering of the LH wave in $k_\perp$. The control of the power decay length by SOL turbulence may not be a good approach because the turbulence in SOL reduces the LHCD efficiency, which is demonstrated in Alcator C-Mod experiment. Therefore, the detachment has been recognized to be a solution to reduce the heat load at the strike point. The experiment for the transition from attached condition to the detachment condition has been made in tokamaks (DIII-D, Alctor C-mod) and helical plasma (LHD and Wendelstein 7-X). Impurity seeding experiments performed in Wendelstein 7-X and TCV demonstrate that impurity seeding is a useful tool to enhance the detachment as well as to reduce the heat flux. The isotope effect on the sputtering has been investigated in JET. It was found that the tungsten sputtering is recognized to be a serious problem in the D-T mixture plasma such as ITER.

Several interesting results on the coupling between the energetic particle and MHD instability, EP-driven turbulence and fast ion confinement, SOL turbulence and current drive efficiency, SOL turbulence and heat load on the divertor plate have been presented in this conference. Deeper understanding of these couplings will be essential for the sustainment of high performance steady-state plasma in ITER

VI. ACKNOWLEDGMENTS

It is a great pleasure to thank all of the contributors for their outstanding achievements, in particular, Dr. E. Ascasibar, Dr. S. Brezinsek, Dr. S. Coda, Dr. F. Effenberg, Dr. A. Ekedahl Dr. X. Gong, Dr. H. Gota, Dr. G. Grenfell, Dr. T. Happel, Dr. J.R. Harrison, Dr. C. Hidalgo, Dr. J. Huang, Dr. Y. In, Dr. A. E. Järvinen, Dr. E. Joffrin, Dr. M. Kaye, Dr. Ye.O. Kazakov, Dr. H. Laqua, Dr. P. Lauber, Dr. A. Leonard, Dr. T.C. Luce, Dr. E.H. Martin, Dr. H.F. Meyer, Dr. S. Ohdachi, Dr. T. Oishi, Dr. H. Park, Dr. C. Paz-Soldan, Dr. T.S. Pedersen, Dr. C. Petty, Dr. M. Podestà, Dr. L. Soto, Dr. B.N. Wan, Dr. M. Xu, Dr. S. Yamamoto, who provided the author with the materials from their presentations and useful informations.

[1] Lauber PH. *et al.* Strongly non-linear energetic particle dynamics in ASDEX Upgrade scenarios with core impurity accumulation. Preprint: 2018 IAEA Fusion Energy Conference, Gandhinagar [EX/1-1].
[2] Thome K.E. *et al.* HighI-frequency energetic particle driven instabilities and their implications for burning plasmas. Preprint: 2018 IAEA Fusion Energy Conference, Gandhinagar [EX/P6-29]
[3] Thome K.E. *et al. Nucl. Fusion* **59** 086011 (2019).
[4] Paz-Soldan C. *et al. Nucl. Fusion* **59** 066025 (2019).
[5] Lvovskiy A., *et al. Plasma Phys. Control. Fusion* **60** 124003 (2018).
[6] Spong, D.A. *et al. Phys. Rev. Lett.* **120** 155002 (2018).
[7] Ohdachi S. *et al.* Excitation mechanism of the energetic particle driven resistive interchange mode and strategy to control the mode in Large Helical Device. Preprint: 2018 IAEA Fusion Energy Conference, Gandhinagar [EX/1-3Rb].
[8] Yamamoto S. *et al.* Impact of ECH/ECCD on fasion-driven MHD instabilities in helical plasmas. Preprint: 2018 IAEA Fusion Energy Conference, Gandhinagar [EX/1-3Ra].
[9] Xu M. *et al.* 2019 *Nucl. Fusion* in press https://doi.org/10.1088/1741-4326/ab1d84.
[10] Yoon S.W. *et al.* The effect of electron cyclotron heating on thermal and fast-ions transport in high beta-poloidal discharges at KSTAR. Preprint: 2018 IAEA Fusion Energy Conference, Gandhinagar [EX/P7-5].
[11] Van Zeeland M.A. *et al. Nucl. Fusion* **56** 112007 (2016).
[12] Galdon-Quiroga J., *et al.* Impact of an edge resonant transport layer on fast-ion confinement in the ASDEX upgrade tokamak. Preprint: 2018 IAEA Fusion Energy Conference, Gandhinagar [EX/P8-26].
[13] Garcia-Munoz M., *et al. Plasma Phys. Control. Fusion* **61** 054007 (2019).
[14] Petty, C.C., *et al. Nucl. Fusion* **59** 112002 (2019).
[15] Podesta, M., *et al.* 2019 *Nucl. Fusion* in press https://doi.org/10.1088/1741-4326/ab3112.
[16] Bardoczi, L., *et al. Plasma Phys. Control. Fusion* **61** 055012 (2019).
[17] Heidbrink, W.W., *et al. Nucl. Fusion* **58** 082027 (2018).
[18] Heidbrink, W.W., *et al. Phys. Plasmas* **24** 056109 (2017).
[19] Van Eester, D., *et al. EPJ Web. Conf.* **157** 03061 (2017).
[20] Kazakov Ye.O, *et al. Nat. Physics* **13** 973 (2017).
[21] Ongena J., *et al. EPJ Web. Conf.* **157** 02006 (2017).
[22] Kazakov Ye.O, *et al.* Recent advances in ICRF heating of mixture plasmas: survey of JET and AUG experiments and extrapolation to JET-DT and ITER. Preprint: 2018 IAEA Fusion Energy Conference, Gandhinagar [EX/8-1].
[23] Joffrin, E., *et al.* 2019 *Nucl. Fusion* in press https://doi.org/10.1088/1741-4326/ab2276.
[24] Laqua H.P., *et al. EPJ Web of Conferences* **203** 02002 (2019).
[25] Coda, S., *et al.* 2019 *Nucl. Fusion* in press https://doi.org/10.1088/1741-4326/ab25cb.
[26] Maurizio, R., et al., *Nucl. Fusion* **58** 016052 (2018).
[27] Jia, M., *et al. Phys. Plasmas* **25** 056102 (2018).
[28] Sun, Y., *et al.* Dynamic ELM and divertor control using mixed toroidal harmonic resonant magnetic perturbations in DIII-D and EAST. Preprint: 2018 IAEA Fusion Energy Conference, Gandhinagar [EX/7-2].
[29] In, Y., *et al.* Test of the ITER-like RMP configurations for ELM-crash-suppression on KSTAR. Preprint: 2018 IAEA Fusion Energy Conference, Gandhinagar [EX/7-1].
[30] Happel, T., *et al.* Advances in the understanding of the I-mode confinement regime: access, stationarity, edge/SOL transport and divertor impact. Preprint: 2018 IAEA Fusion Energy Conference, Gandhinagar [EX/2-3].
[31] Happel, T., *et al. J. Nucl. Mat.* **18** 159-165 (2019).
[32] Ida, K., *et al. Phys Rev Lett* **120** 245001 (2018).
[33] Grenfell, G., *et al.* 2019 *Nucl. Fusion* in press https://iopscience.iop.org/article/10.1088/1741-4326/aaf034.
[34] Harrison, J.R., *et al. Nucl. Fusion* **59** 112011 (2019).
[35] Harrison J. R. ,*et al. Phys. Plasmas* **22** 092508 (2015).
[36] Scotti F., *et al. Nucl. Fusion* **58** 126028 (2018).
[37] Kaye, S.M., *et al. Nucl. Fusion* **59** 112007 (2019).
[38] Samuell, C., *et al. Phys. Plasmas* **25** 056110 (2018).
[39] Leonard, A.W., *et al.* Parallel energy transport in detached DIII-D divertor plasmas. Preprint: 2018 IAEA Fusion Energy Conference, Gandhinagar [EX/P6-12].
[40] Oishi, T., *et al.* Effect of deuterium plasmas on carbon impurity transport in the edge stochastic magnetic field layer of Large Helical Device. Preprint: 2018 IAEA Fusion Energy Conference, Gandhinagar [EX/P3-11].
[41] Martin, E.H., *et al.* Experimental evidence of lower hybrid wave scattering in Alcator C-mod due to scrape off layer density fluctuations. Preprint: 2018 IAEA Fusion Energy Conference, Gandhinagar [EX/8-2].
[42] Martin, E.H., *et al. Nucl. Fusion* **59** 076006 (2019).
[43] Baek, S.G., *et al. Phys. Rev. Lett.* **121** 055001 (2018).
[44] Baek, S.G., *et al.* Recovery of efficient lower hybrid current drive at a low Greenwald fraction in Alcator C-mod high density plasmas. Preprint: 2018 IAEA Fusion Energy Conference, Gandhinagar [EX/P6-28].
[45] Sunn Pedersen *et al.* First divertor physics studies in Wendelstein 7-X. Preprint: 2018 IAEA Fusion Energy Conference, Gandhinagar [EX/9-1].
[46] Sunn Pedersen *et al.* 2019 *Nucl. Fusion* accepted.
[47] Zhang , D *et al.Phys. Rev. Lett.* **123** 025002 (2019).
[48] Kobayashi, M., *et al.* 2019 *Nucl. Fusion* in press https://doi.org/10.1088/1741-4326/ab26e6.
[49] Jaervinen, A.E., *et al. Phys. Rev. Lett.* **121** 075001 (2018).
[50] Jaervinen, A.E., *et al.* Progress in DIII-D towards validating divertor power exhaust predictions. Preprint: 2018 IAEA Fusion Energy Conference, Gandhinagar [EX/9-3].
[51] Guo, H.Y., *et al. Nucl. Fusion* **57** 044001 (2017).
[52] Marcinko, S. *et al. Phys. Plasmas* **25** 022507 (2018).
[53] Sahoo, B.P., *et al. Phys. Plasmas* **24** 082505 (2017).
[54] Effenberg, F., *et al.* Demonstration of power exhaust control by impurity seeding in the island divertor at Wendelstein 7-X. Preprint: 2018 IAEA Fusion Energy Conference, Gandhinagar [EX/9-2].
[55] Effenberg, F., *et al.* Demonstration of power exhaust control by impurity seeding in the island divertor at Wendelstein 7-X, submitted to NF January 2019.
[56] Theiler, C., *et al.* SOL transport and detachment in alternative divertor configuration in TCV L- and H-mode plasmas. Preprint: 2018 IAEA Fusion Energy Confer-

ence, Gandhinagar [EX/P1-19].
[57] Christen N., *et al. Plasma Phys. Control Fusion* **59** 105004 (2017).
[58] Kirschner A., *et al.*, *Plasma Phys. Control Fusion* **60** 014041 (2018).
[59] Brezinsek, S., *et al.* 2019 *Nucl. Fusion* in press https://doi.org/10.1088/1741-4326/ab2aef.
[60] Eckstein W. *Top. Appl. Phys.* **110** 33 (2007).
[61] Gota, H., *et al. Nucl. Fusion* **59** 112009 (2019).
[62] Ono, Y., *et al. Nucl. Fusion* **59** 076025 (2019).